

Fatigue Behaviour of High Velocity Oxy-Fuel Coatings on Medium Carbon Steel

M. A. M. Halmi¹, M. A. Harimon², A. E. Ismail³, D. Chue⁴

¹Research Scholar, Faculty of Mechanical and Manufacturing Engineering, Universiti Tun Hussein Onn Malaysia, Malaysia

²Lecturer, Faculty of Mechanical and Manufacturing Engineering, Universiti Tun Hussein Onn Malaysia, Malaysia

³Associate Professor, Faculty of Mechanical and Manufacturing Engineering, Universiti Tun Hussein Onn Malaysia, Malaysia

⁴Engineer, Metatech Sdn Bhd, Malaysia

¹ariffhalmi91@gmail.com, ²mazhar@uthm.edu.my, ³emran@uthm.edu.my

Abstract — Nowadays, the application of high-velocity oxy-fuel (HVOF) thermal spraying coating is widely used in various industries. This is due to its ability to improve the wear, erosion, and corrosion resistance of components. However, by taking consideration of fatigue behaviour into cognisance, the consequence of the HVOF thermal spraying coating on the components remains debatable. In this research, the fatigue behaviour of the uncoated steel, WC-12Co coated steel, and WC-10Ni coated steel were investigated. At first, the tensile test was conducted on the S50C steel to determine its yield strength. The yield strength was then being applied as a benchmark in a staircase method to set the stress amplitudes for the fatigue test. Fatigue tests were performed under the stress ratio, $R=-1$, by tension-compression cyclic loading (sine wave) with a frequency of 20 Hz according to ASTM-E466. The results showed that the HVOF decreased the tensile and yield strength by 8.9% and 9.5%, respectively. Similar behaviours are shown by the fatigue properties, as the HVOF coated steel reduced the fatigue strength's by 17%. The decrement of the fatigue strength was mainly due to the increment of the substrate's grain size, which results from the high flame temperature (2750°C) of the HVOF process.

Keywords — fatigue, HVOF, S50C carbon steel, WC-12Co, WC-10Ni.

I. INTRODUCTION

The high-velocity oxy-fuel coating is the most current developed process of thermal spray coating during the 1980s. It was developed from the conventional flame spray process but with a higher spraying velocity [1]. The specific characteristic of higher particle velocity and lower particle temperature by the HVOF process is attributed to higher coating density, lower porosity, and less decarburization [2]. In industrial applications, the HVOF deposition process is used to enhance wear, erosion, and corrosion resistance. Particularly, WC-12Co high-velocity oxy-fuel coating is deposited to improve the wear resistance of components with the help of cobalt metal binder [3]. Meanwhile, nickel-metal binder in the WC-10Ni coatings is attributed to the corrosion resistance of the component [4].

On fatigue properties, most researchers have a similar conclusion stating that HVOF coating decreased the fatigue strength of the substrates, but they submitted it for different reasons. The reasons are the existence of the high tensile residual stress on the surface coating [5], high microcrack density [6], strong adhesion strength between substrate and coating [7], high coatings porosity [8], presence of stress concentrators at the interface [9], etc. External surroundings such as corrosive environments [10] and high temperature [11] also affect the fatigue strength of the components. Some improvement of the fatigue strength can be achieved with the help of grit blasting treatment [12], shot peening treatment [13], or annealed treatment [14].

Based on previous researches [15-18], most studies focused on the coating, which acts as a prime cause of the failure. However, the focus of this study is on the substrate. The effects of the HVOF process on the fatigue behaviour of the steel substrate were analyzed. In addition, this research investigated the relationship between tensile strength and fatigue strength. Also, this paper provides the fractographic analysis of the fractured specimen.

II. EXPERIMENTAL

A. Materials

In this research, the coating powders used in the present work are WC-12Co and WC-10Ni. Both powders will produce a good bond strength and hard, dense coating. WC-12Co coatings are typically used in wear applications due to the presence of 88% of tungsten carbide as a hard material and 12% of cobalt matrix functions as a binder material for the carbide particle, which also improves the toughness of coatings [19]. Meanwhile, WC-10Ni coatings are typically used in corrosive applications due to proven better corrosion resistance compared to WC-Co coatings [20]. The substrate used in this research is S50C medium carbon steel. The S50C steel is good weldability, good machinability, high strength, and high impact properties. Table I shows the chemical composition of S50C steel, WC-12Co powder, and WC-10Ni powder.



Table I: Chemical composition of S50C steel, WC-12Co powder, and WC-10Ni powder

Type	Weight (%)	
	S50C steel	Fe
C		0.52
Si		0.27
Mn		0.64
P		0.016
S		0.004
WC-12Co powder	W	Balance
	Co	12.09
	C	5.18
	Fe	0.65
WC-10Ni powder	W	Balance
	Ni	10.21
	C	5.17
	Fe	0.68

B. Specimen preparation

The S50C steel was machined into a specific specimen's dimension using CNC milling. For tensile and fatigue tests, the S50C steel was machined into a dog bone-shaped, as in Fig. 1, in accordance with ASTM E8/E8M [21] and ASTM E466 [22]. For microstructure and grain size analysis, the S50C steel was machined into cuboid-shaped, as in Fig. 2.

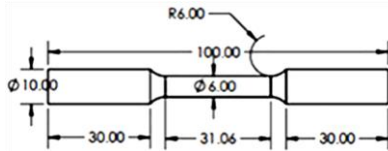


Fig. 1: The dimension of a dog-bone shaped specimen (in mm)

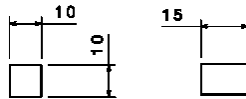


Fig. 2: The dimension of a cuboid-shaped specimen (in mm)

Prior to coating's deposition, the substrate was cleaned with acetone to remove oil, grease, dirt, mill, and rust scale. Next, the substrate was grit blasted by using Shipblast 600Lbs. Aluminum silicate, Al₂SiO₅ (also known as coal slag) with a 20-40 mesh size, was used as the abrasive material for the grit-blasting process. The purpose of this process is to remove any contaminants on the surface of the substrate in order to produce a clean surface for the coating's deposition. On top of that, the process of grit blasting will also produce surface roughness, ensuring mechanical anchoring between the coating and the surface of the substrate [23].

ZB-2000 Mobile HVOF with Diamond Jet DJ2700 gun of Bexxon was used to spray the HVOF coating powder at very high speed, 2150 ms⁻¹ with lower temperature, 2750°C, in order to produce a hard dense and porous free coating. The coating powder was first preheated to ensure the chemical group in the powder react together to polymerize each other and to enhance the coating's performance. For a dog-bone-shaped specimen, the coating will be covered at the middle section of the specimen, whereas for a cuboid-shaped specimen, the coating will be covered at one side of the specimen. The coating's parameter will be set constant for every specimen, as in Table II.

Table II: Coating's parameter

Parameter	Value
Thermal spray gun	The Diamond Jet DJ2700 of Bexxon
Powder feeding rate (g/min)	15-150
Particles size (µm)	45±15
Oxygen pressure (MPa)	1.2
Fuel pressure (MPa)	0.62
Air pressure (MPa)	0.72
Air flow (L/min)	440
Fuel flux (L/min)	88
Oxygen flux (L/min)	310
Spraying distance (mm)	200-250
Coating thickness (mm)	0.25

C. Microstructure analysis

An optical microscope (OM) and a scanning electron microscope (SEM) were used to observe the microstructure of the specimens. The optical microscope used in this study is Olympus BX60M. This type of microscope has a magnification range of only 5x to 100x, which has its limitation when viewing a structure. Therefore, the scanning electron microscope is a better microscope to observe a higher magnification structure.

D. Grain size analysis

Prior to the grain size analysis, the specimen underwent a ground, polished, and etching process for a visible and unscratched image. Then, the specimen was put under the optical microscope to capture the grain's image in a specific position, as in Fig. 3 and Fig. 4. The specific position is located at the substrate region (which is 0.5 mm from the interface) to ensure that the alteration of S50C steel grain's size before and after the HVOF thermal spray coating can be observed.

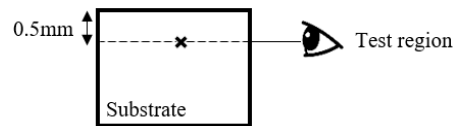


Fig. 3: Region of the grain image captured for uncoated steel

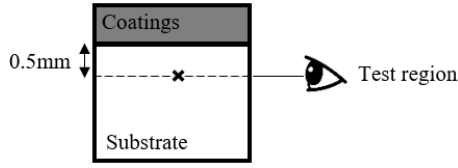


Fig. 4: Region of the grain image captured for WC-12Co and WC-10Ni coated steel

The images taken were then analyzed using the ImageJ software for the grain size calculation. Method for measuring the grain size distribution is by using intercept-method, where it considers a line along with the micrograph image and calculated how many intersecting points with the grain boundaries. The average grain size value from all lines was taken for the final result [24].

E. Tensile test

The purpose of a tensile is to obtain the yield strength for the benchmark in the fatigue test. It also investigates the tensile properties of the substrate after the HVOF process taken place. The tensile test was conducted following ASTM E8/E8M [21] at room temperature. The crosshead speed setting was 0.5 mm/min. The load and elongation were recorded from the test machine; meanwhile, stress and strain values were calculated. Both substrate and coating diameters were included in the cross-sectional region of the specimen used to measure the tensile properties.

F. Fatigue test

The purpose of a fatigue test is to determine the fatigue strength from a material subjected to cyclic loading. The fatigue test was conducted in an axial fatigue test, under the load controlled (load ratio, R=-1) by tension-compression cyclic loading (sine wave) in accordance with ASTM E466 [22]. The load frequency was set up at 20 Hz, and the predetermined cycle was determined at 10⁶ cycles.

To estimate the fatigue strength by taking into account its statistical nature, the staircase method (up and down method) was used for this test [25]. By staircase method, the test was conducted with a range of the number of different load amplitude obtained by calculations. On the first calculation, the result from the previous tensile test, as in Table III, are calculated on average. The yield strength's values of uncoated steel, WC-12Co coated steel, and WC-10Ni coated steel were calculated in averaged value, as in (1).

$$R_{p0.2(avg.)} = \frac{R_{p0.2(uncoated)} + R_{p0.2(wc-co)} + R_{p0.2(wc-ni)}}{3} \quad (1)$$

Also, the area of the previous tensile specimens for uncoated steel, WC-12Co coated steel, and WC-10Ni coated steel were calculated in averaged value, as in (2).

$$A_{(avg.)} = \frac{A_{(uncoated)} + A_{(wc-co)} + A_{(wc-ni)}}{3} \quad (2)$$

The first designation load amplitude $F_{a(1st)}$ was calculated from the 55% of average yield strength (811 MPa) and averaged area (31.6 mm²) by the nominal stress formula, as in (3). The 55% percentage is the expected value of the fatigue strength, according to Y. Murakami [26].

$$F_{a(1st)} = 55\% \times R_{p0.2(avg.)} \times A_{(avg.)} \quad (3)$$

For the next calculation of load amplitude $F_{a(n)}$, the arithmetic progression method was applied with the first term is the calculated first load amplitude, a is 13.5 kN, n is the number of terms and common difference, d is -1.5 kN, as in (4). The result of the fatigue test produced a stress-number of the cycle (S-N) curved.

$$F_{a(n)} = a + (n - 1) d \quad (4)$$

G. Fractographic analysis

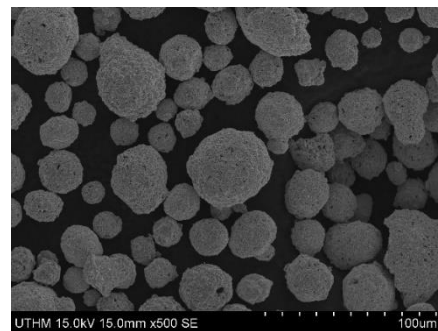
After the tensile and fatigue test were completed, the fractured specimens were sectioned 20 mm from the fractured surface using an electric angle grinder. Next, the specimens underwent fractographic analysis using the scanning electron microscope. The fractographic analysis was aimed to determine the cause of failure in fractured surfaces by studying the characteristics of the fractured surfaces.

III. RESULTS AND DISCUSSION

A. Microstructure analysis

The detailed powder manufacturing method affects the powder characteristics such as particle shape, structure, and size, powder density, flowability, purity, phase content, etc. The SEM micrographs of WC-12Co powder and WC-10Ni powder can be seen in Figure 5 and Figure 6. Both powders showed an identical microstructure, consists of small spheroidal evenly distributed particles. This proved that both powders are agglomerated and sintered powders.

According to B. Wielage *et al.*, granules morphology analysis for agglomerated and sintered powder revealed that they are characterized mostly by a spherical shape, whereas sintered and crushed powder are characterized mostly by irregular shape, where it has poorer flowability compared to spherical shaped powder [27].



(a)

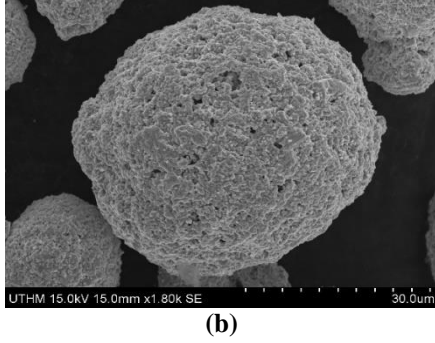


Fig. 5: The micrograph image of WC-12Co powder with a magnification of; (a) 500x, (b) 1800x

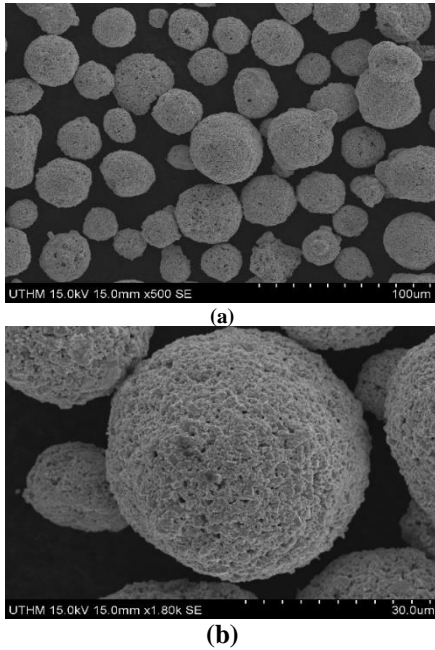


Fig. 6: The micrograph image of WC-10Ni powder with a magnification of; (a) 500x, (b) 1800x

Fig. 7, Fig. 8, and Fig. 9 display the surface morphology of the S50C steel substrate, WC-12Co coatings, and WC-10Ni coatings. It showed that the distribution of tungsten carbide (WC) consists of an angular shape and, in light contrast, dissolves into a metallic binder of Co and Ni, which is in dark contrast. During the HVOF process, WC carbide grain is preferentially melted in both binder phases at high temperatures [28]. According to J. M. Guilemany *et al.* [29], the heating process above the melting point of the powder is the main factor for the molten WC to dissolve binder matrix Co and Ni rapidly, forming CoWC and NiWC liquid alloys.

Pores have been observed on the coating's surface due to the random build-up, curling up, and incomplete filling of splats' interstices during the thermal spray process. This will degenerate the bonding strength, accommodate deformation, accelerate crack propagation and worsen the mechanical

performance of the coatings [30]. It was reported that the level of porosity depends on the flame temperature. A lower flame temperature produces more pores compared to a higher flame temperature process. Therefore, the lower flame temperature in HVOF compared to other thermal spray processes makes a number of pores inevitable [31].

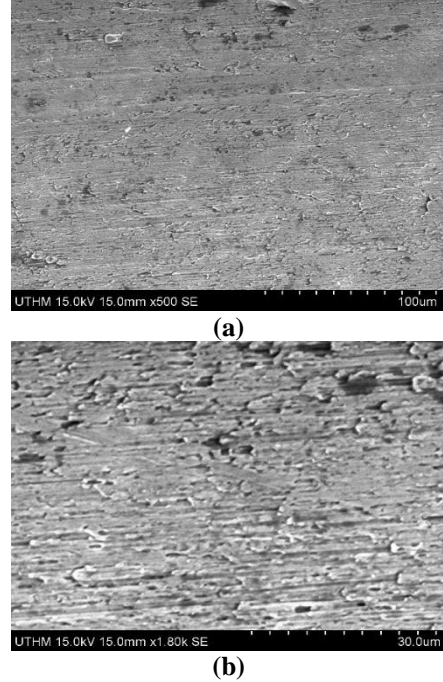


Fig. 7: The micrograph image of S50C steel with a magnification of; (a) 500x, (b) 1800x

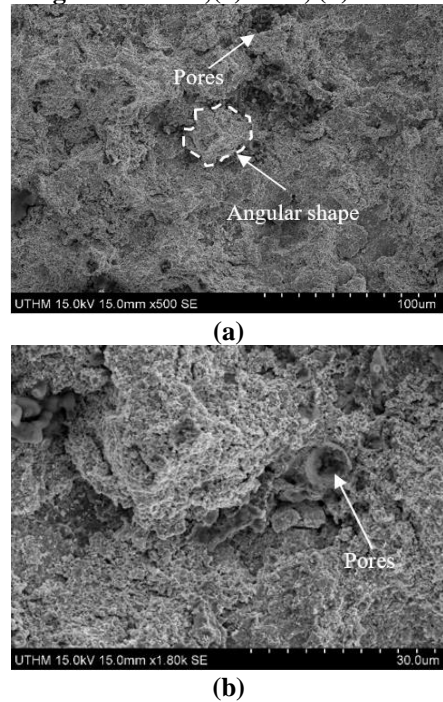


Fig. 8: The micrograph image of WC-12Co coating with a magnification of; (a) 500x, (b) 1800x

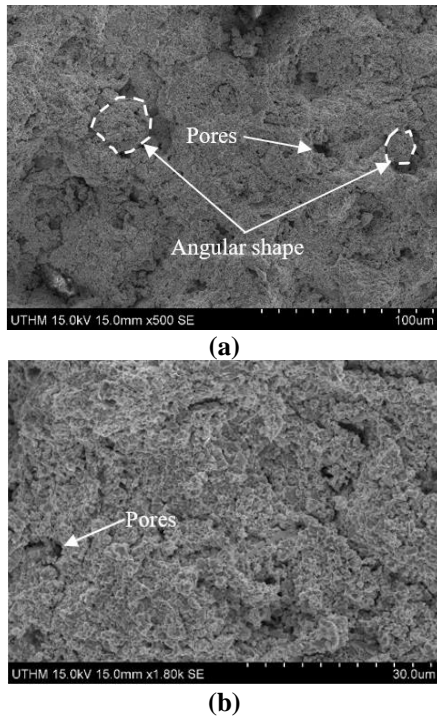


Fig. 9: The micrograph image of WC-10Ni coating with a magnification of; (a) 500x, (b) 1800x

Fig. 10 shows the cross-sectional micrograph of the WC-12Co and WC-10Ni coatings observed by SEM. Strong adhesion between the dense coating layer and the substrate was revealed in the cross-sectional micrograph. However, some extreme plastic deformation and swift solidification are followed by the high-velocity effect of coating powders on the substrate's surface. The coating layers are also likely to have unavoidable pores and cracks. [32]. According to N. W. Satya [33], on the coated steel, a common 1.89 percent porosity was identified, and the unbonded interface between the coating and the substrate was around 38 percent long. Cracks were also found on the substrate's surface, which caused not only by the high impact of powder particle, but it also caused by the grits from grit blasting treatment.

From the observation, both coatings consist of a lower number of pores and semi-melted particles. The presence of semi-melted particles is due to the HVOF spraying process, where the powdered particles experienced thermal and kinetic history, causing the particles to impinge on the substrate in partially molten or fully molten [34]. M. Jadidi [35] supported that velocity, trajectory, temperature, and melting state, have a tremendous influence on the coating properties. Clearly, by HVOF, a low flame temperature and very high particle velocity caused the presence of semi-molten particles.

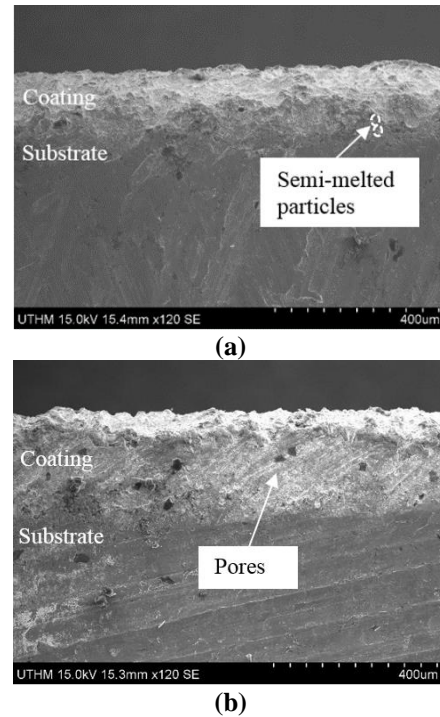


Fig. 10: The cross-sectional micrograph image of; (a) WC-12Co coating, (b) WC-10Ni coating with a magnification of 120x

B. Grain size analysis

There was an increment of grain size by the substrate at the WC-12Co and WC-10Ni coated steel, as in Fig. 11. The average grain size of the uncoated steel was 40.3 μm . Meanwhile, the average grain size at the substrate of the WC-12Co and WC-10Ni coated steel increased to 61.3 μm and 60.3 μm , as in Fig. 12. These growths of the grain are mainly due to the high-temperature effect (2750°C) from the HVOF thermal spray process, which alters the original grain size of the S50C substrate. According to Callister and Rethwisch [36], if the material is left at an elevated temperature, the grains will begin to grow. The total boundary area decreases as grains increase in size, yielding a concomitant decrease in the total energy; this is the driving force for grain growth. Heat treatment also provides an effective way to manipulate the properties of the metal by regulating the rate of diffusion and the rate of cooling inside the microstructure, according to Zia *et al.* [37]. The mechanical properties of a metallic alloy can be altered by heat treatment, which manipulates properties such as hardness, strength, ductility, and elasticity.

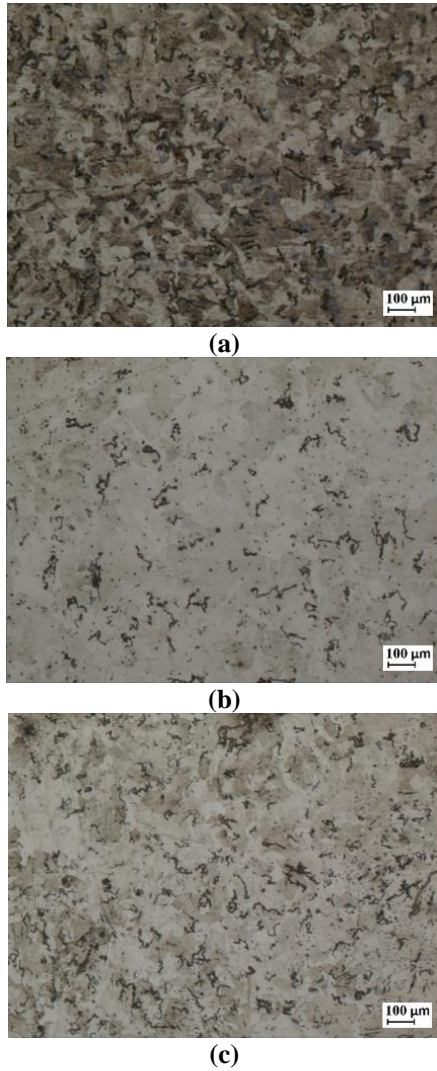


Fig. 11: Grain micrograph image of; (a) uncoated steel, (b) WC-12Co coated steel (at substrate), (c) WC-10Ni coated steel (at substrate)

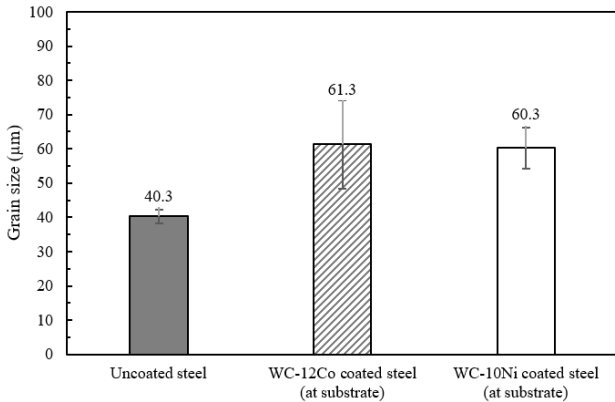


Fig. 12: Grain size for uncoated steel, WC-12Co coated steel (at substrate), WC-10Ni coated steel (at substrate)

C. Tensile test

The load versus elongation curve was converted into a stress-strain curve by taking into consideration the additional thickness and cross-sectional area of the coating deposition, with overall stress calculated by the instantaneous load over the initial area, as in Fig. 13. By comparing the coated steel with the uncoated steel in Table III, the WC-12Co coated steel (782 MPa) and WC-10Ni coated steel (825 MPa) have a lower tensile strength value compared with the uncoated steel (858 MPa). Similar to the yield strength properties, the value of the yield strength is lower on the WC-12Co coated steel (766 MPa) and WC-10Ni coated steel (821 MPa) compared to the uncoated steel (846 MPa). This showed that the impact of the HVOF process lowered the S50C steel's tensile strength and yield strength.

The decrement of tensile strength and yield strength was because of the hardening effect, specifically, the increment of the grain size at the substrate's surface, as in Fig. 14. The increment is due to the 2750°C high-temperature effect of the HVOF process, which was directly sprayed onto the substrate's surface. As the grain size grew, the number of dislocations stacked up at the grain boundary was affected, as the grain boundary served as a dislocation motion barrier. The coarser-grained material has a smaller total grain boundary area to hinder dislocation movement; thus, the coarse-grained material is weaker than the fine-grained material. This has made the coarse-grained material less resistant to plastic deformation, resulting in lower tensile and yield strength values [36].

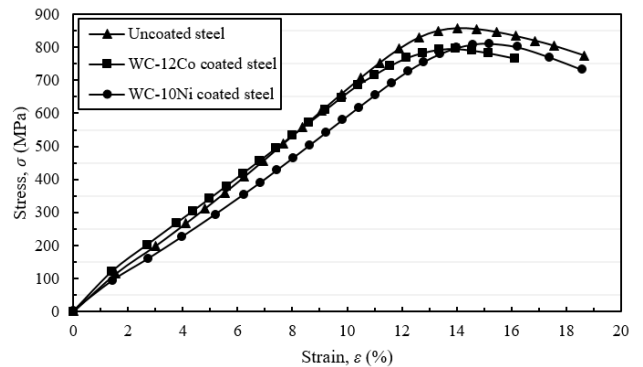


Fig. 13: Stress-strain curves of uncoated steel, WC-12Co coated steel, and WC-10Ni coated steel

Table III: The tensile properties value of uncoated steel, WC-12Co coated steel, and WC-10Ni coated steel

	Specimen		
	Uncoated steel	WC-12Co coated steel	WC-10Ni coated steel
Tensile strength, σ_u (MPa)	858	782	825
Yield strength, $R_{p0.2}$ (MPa)	846	766	821

	Specimen		
	Uncoated steel	WC-12Co coated steel	WC-10Ni coated steel
Elastic modulus, E (MPa)	6605	6036	5635
Total strain, ϵ (%)	20.7	18.5	21.3
Max load, F_a (kN)	24.3	24.2	25.6
Total elongation, ΔL (mm)	6.44	5.75	6.61

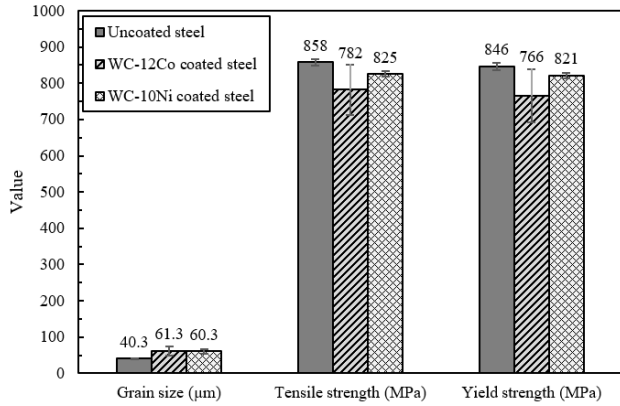


Fig. 14: The relation between grain size, tensile strength, and yield strength

However, the percentage of tensile and yield strength's decrement is very low. The percentage of tensile strength decrement by WC-12Co coated steel is 8.9% and by WC-10Ni coated steel is 3.9%. Meanwhile, the percentage of yield strength decrement by WC-12Co coated steel is 9.5% and by WC-10Ni coated steel is 3%. These low decrements are due to the very small thickness of the coatings used (0.15 mm, 0.25 mm, and 0.35 mm) compared with the diameter of the substrate, which is 6 mm, hence, making the tensile behavior of the coatings of little influence when compared to the overall tensile behavior. Furthermore, cracks in the coating surface were observed before the plastic deformation of the steel during the tensile test. The coating has fractures from the steel while the overall tensile curve was still within the elastic region. Fig. 15 shows the cracks of the coatings during the tensile test.



Fig. 15: Crack in coatings within the elastic deformation of the specimen during tensile loading

On the other hand, there was no significant effect on the elastic modulus and total strain properties due to the HVOF process, as there is no constant trend (constant increase or decrease) in their values.

D. Fracture mechanism

A moderate amount of necking, followed by the formation of voids, cracks, and shears, precedes fractures in the most ductile metal. This gives the uncoated steel and coated steel with WC-12Co and WC-10Ni coatings the characteristic cup-and-cone fracture, as in Fig. 16. There is also irregular and fibrous appearance in the central interior region, as shown in Fig. 17, which implies that there had been mechanisms of plastic deformation [38].



(a)



(b)



Fig. 16: The fractured surface of; (a) uncoated steel, (b) WC-12Co coated steel, (c) WC-10Ni coated steel

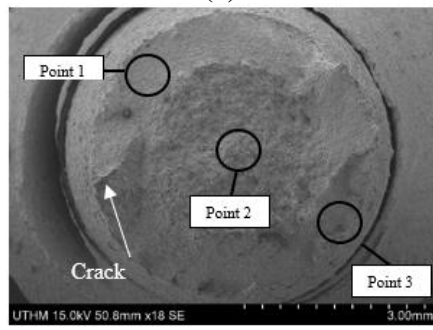
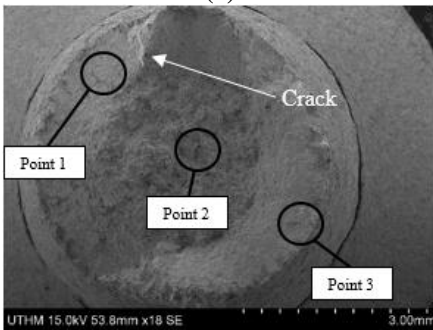
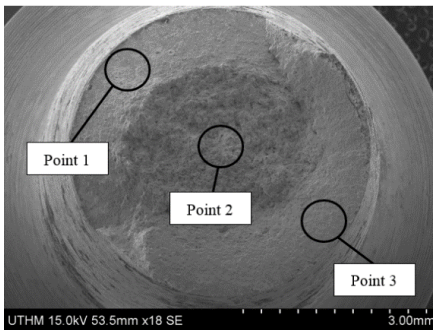
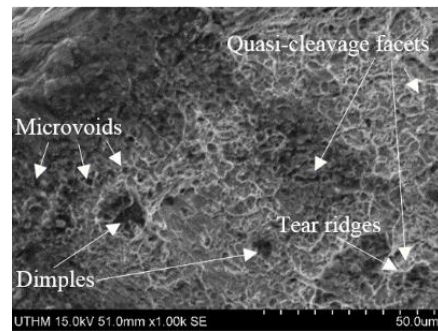


Fig. 17: The fractured surface of; (a) uncoated steel, (b) WC-12Co coated steel, (c) WC-10Ni coated steel with a magnification of 18x

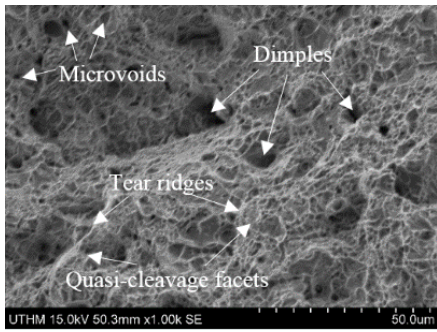
Analysis of the results from SEM shows that both uncoated and WC-12Co/WC-10Ni coated steel showed no significant difference on the fractured surface. Fig. 18, Fig. 19, and Fig. 20 represent the SEM images of the fractured tensile specimen at different points (Point 1, Point 2, and Point 3), as labeled in Fig. 17. The detailed view of the fractured surface is characterized by the microvoids, tear ridges, transgranular ductile dimples, and transgranular quasi-cleavage facets. However, the fractured surface mainly consists of ductile dimple tearing, a consequence of the microvoid coalescence and few percentages of transgranular quasi-cleavage facets. Nonetheless, the overall fracture occurred in a transgranular manner, as most cracks are propagated through the grains.

In the detailed view, Point 2 of both coated and uncoated steel show a higher number of ductile dimples compared with other points. This indicates that the ductile fracture mechanism, which is characterized by a considerable amount of plastic deformation before and during crack propagation, occurred at the center of the specimen (Point 2). With respect to tensile loading, Pandey *et al.* [39] stated that the coalescence of microvoids results in equiaxed dimples on the surface of ductile tensile fracture normal to the loading axis. Therefore, on a flat crater bottom-loaded by tension, it reveals the equiaxed and spherical dimples and elongated ellipsoidal dimples on the shear lips oriented at 45°.

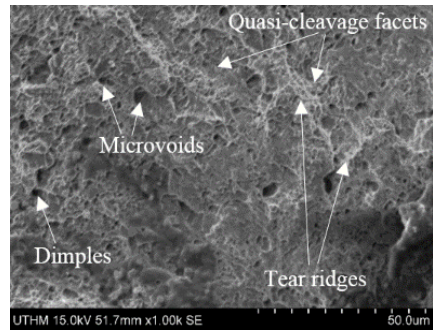
The amount of nonlinear nature of microscopic cracks intermingled with pockets of cleavage facets was increased in the outer region, either Point 1 or Point 3 compared to Point 2. The cleavage facets indicate that “locally” brittle fracture mechanism, which is characterized by micro-deformation or no gross deformation during the crack propagation, occurs at these regions. The small region of the tensile specimen fractured in a brittle manner due to the inability to withstand the very high tensile load, resulting from the low-stress area. According to Yan and Zhao [40], as the stress increases during tensile loading, the cross-sectional area is reduced, and the necked region is produced. Upon observation on the fracture surface comparison, with ductile behavior shown, there is a considerable amount of stress caused where cracks propagated until failure.



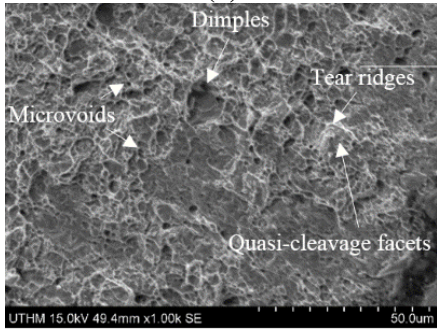
(a)



(b)



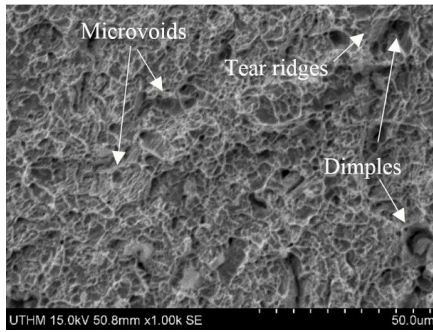
(c)



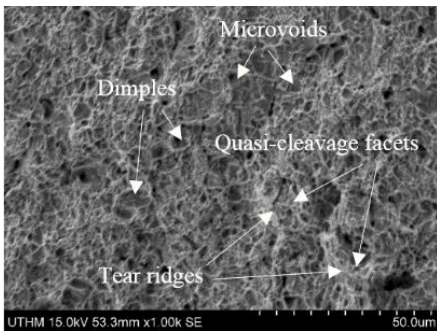
(c)

Fig. 19: The fractured surface of WC-12Co coated steel with a magnification of 1000x at; (a) Point 1, (b) Point 2, (c) Point 3

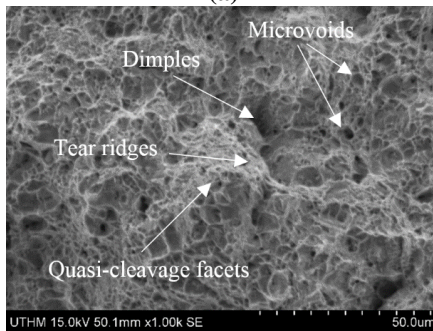
Fig. 18: The fractured surface of uncoated steel with a magnification of 1000x at; (a) Point 1, (b) Point 2, (c) Point 3



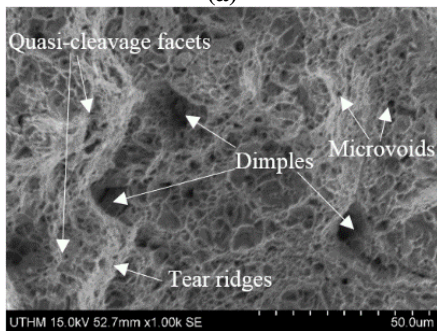
(a)



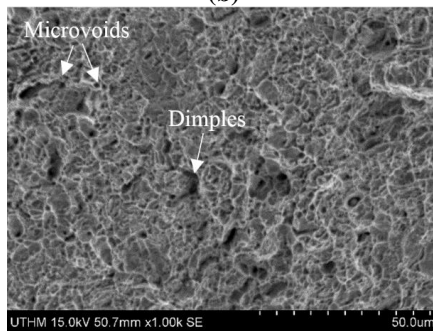
(a)



(b)



(b)



(c)

Fig. 20: The fractured surface of WC-10Ni coated steel with a magnification of 1000x at; (a) Point 1, (b) Point 2, (c) Point 3

On the other hand, a visible crack can be seen at the outer region, Point 1 and Point 3 of the fractured steel for both WC-12Co and WC-10Ni coated steel in Fig. 17(b) and Fig. 17(c). This indicates that cracks may be nucleated at the surface of the substrate, Point 1 and Point 3, and transversely propagated inside the central region, Point 2. In previous research, the cracks are thought to be heterogeneously nucleated at sites where further deformation is difficult and consists predominantly of foreign inclusions [38].

As by coated steel, the presence of foreign inclusion contains coating and grit particles on the substrate's surface, resulting in crack deformation at the outer region. These cracks will then be propagated inside the central region. At the same time, a localized reduction in the cross-sectional area, called necking, occurred. After that, numbers of microvoids, cracks, and dimples formed, which then formed a crack growth from the central region at Point 2 outwards perpendicularly to the stress application. Finally, a rapid crack propagation at about 45° to the tensile axis leads to a total brittle fracture. Fig. 21 shows the flow of the fracture mechanism [38].

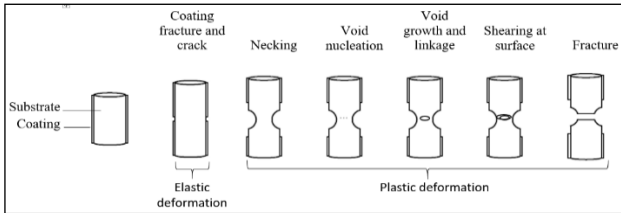


Fig. 21: Schematic diagram of the ductile tensile fracture mechanism

E. Fatigue behavior

Based on Table IV shows that the uncoated steel has the highest fatigue strength (317 MPa at 10⁶ cycles), followed by WC-10Ni coated steel (307 MPa at 10⁶ cycles) and WC-12Co coated steel (263 MPa at 10⁶ cycles). Similar to the lines in Fig. 22, it showed that the uncoated steel's line is located uppermost, followed by WC-10Ni coated steel and WC-12Co coated steel, which explained that the uncoated steel has the highest fatigue strength, followed by the coated steel. Besides that, all lines are parallel to each other proved that no external factors such as temperature, corrosion, etc., affected the specimens during the test.

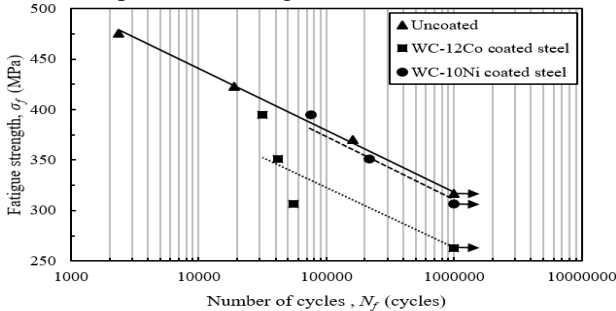


Fig. 22: The stress-life (S-N) diagram of uncoated steel, WC-12Co coated steel, and WC-10Ni coated steel

Table IV: The stress-life (S-N) value of uncoated steel, WC-12Co coated steel, and WC-10Ni coated steel

Specimen	Load amplitude, F_a (kN)	Fatigue strength, σ_f (MPa)	Number of cycles (cycles)
Uncoated steel	13.5	476	2365
	12.0	423	18908
	10.5	370	162151
	9.0	317	1000000
	13.5	476	2365
WC-12Co coated steel	13.5	395	31424
	12.0	351	41796
	10.5	307	54749
	9.0	263	1000000
WC-10Ni coated steel	13.5	395	75048
	12.0	351	214671
	10.5	307	1000000

From Fig. 23, the fatigue strength of WC-12Co coated steel is decreased by 17%, whereas the fatigue strength of WC-10Ni coated steel was decreased by 3.2%. The decrement was due to the 2750°C high-temperature effect of the HVOF coating process directly sprayed onto the substrate's surface, which enlarged the size of the grain. As the grain size enlarged, it increased localized strain along with slip bands, increasing the amount of irreversible slip and provide fewer grain boundaries to aid in transcrystalline crack arrest and deflection, thus raising the growth rate of fatigue crack [41].

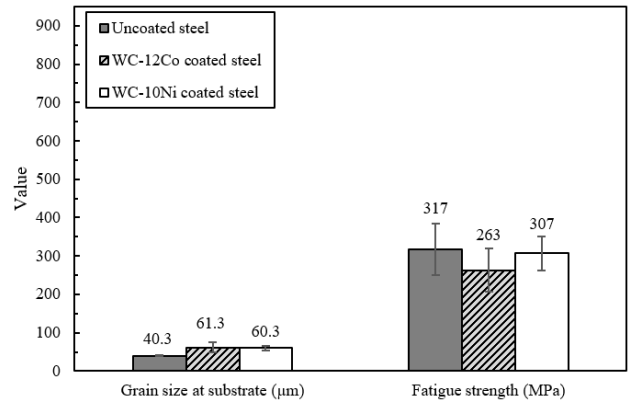


Fig. 23: The relation between grain size and fatigue strength

E. Fatigue ratio

The fatigue strength has a wide range value from 1-70% from its ultimate tensile strength, depending on surface finish, specimen size, load type, temperature, corrosive, mean stresses, residual stresses, stress concentrations, etc. For instance, a material that has a fatigue strength of a 1%

from its ultimate tensile strength is normally high-strength steel with a sharp notch subjected to a high mean tensile stress under a corrosive environment. On the contrary, a material that has a fatigue strength of 70% from its ultimate tensile strength is normally medium strength steel under an inert atmosphere, containing considerable compressive residual stress [41].

In this research, the relationship between fatigue strength and tensile strength can be illustrated in Fig. 24. It shows that the fatigue strength increases correspondingly toward the tensile strength. Also, the averaged fatigue ratio, σ_f/σ_U value, was at about 0.36, which is, however, lower compared to the expected value, 0.5.

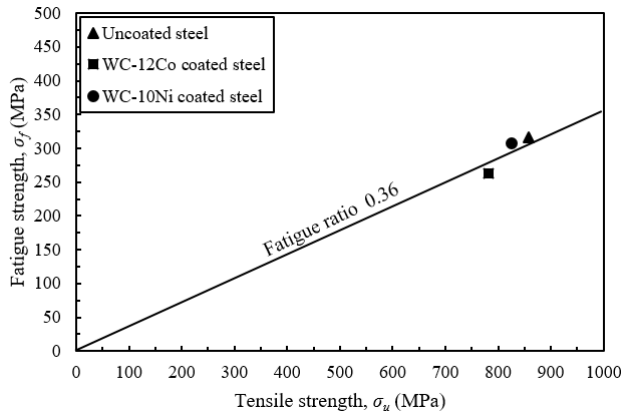


Fig. 24: The relation between fatigue strength and tensile strength

According to S. Kalpakjian [42], common, polished steels have a fatigue strength of 50% from their tensile strength, for a tensile strength value below 1200 MPa, as in (5).

$$\sigma_f \approx 0.5 \sigma_u \text{ for } \sigma_u \leq 1200 \text{ MPa} \quad (5)$$

However, the fatigue ratio in this research was lower than expected. It is due to the surface factor of ‘machined’ steel in the shape of a dog bone specimen. Thus, a correction factor must be considered in the equation, as in (6).

$$\sigma_f \approx 0.5 \times K \times \sigma_u \quad (6)$$

According to R. C. Juvinall and K. M. Marshek [43], taking into consideration of machined steel and an averaged tensile strength of 822 MPa, the correction factor value is in the range of 0.72. Thus, the calculated fatigue strength should be as in (7).

$$\sigma_{f(avg.)} \approx 0.5 \times K \times \sigma_{u(avg.)} \quad (7)$$

$$\sigma_{f(avg.)} = 0.5 \times 0.72 \times 822 \text{ MPa} = 296 \text{ MPa}$$

To prove that this calculation is valid, the value of the

average fatigue strength in the calculation is equal to the average fatigue strength in the experiment, as shown in Table V, which is 296 MPa.

Table V: The fatigue strength and tensile strength value

Specimen	Fatigue strength, σ_f (MPa)	Tensile strength, σ_u (MPa)	Fatigue ratio
Uncoated steel	317	858	0.37
WC-12Co coated steel	263	782	0.34
WC-10Ni coated steel	307	825	0.37
Averaged value	296	822	0.36

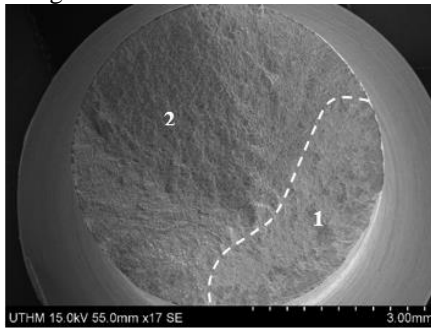
G. Fracture Morphology Observations

The fractured surface can be seen to have two distinct regions, which are burnished, smooth or granular, rough regions. In Fig. 25, Fig. 26, and Fig. 27, the burnished, smooth region was labeled as 1, while the granular, rough region was labeled as 2. The burnished, smooth region is the region where the fatigue crack took place. It consists of cracks initiation, progression mark, clamshell pattern, benchmark, and striation. On the other hand, the granular, rough region is the region where the final ductile fracture occurred. In a fatigue cycle, the final ductile fracture region underwent a fracture in a shorter period compared to the fatigue crack region [44].

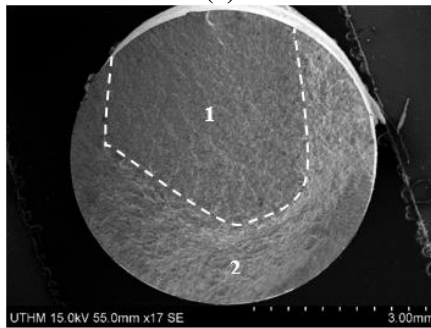
Fig. 25(a), Fig. 25(b), and Fig. 25(c) show the same type of specimen, uncoated steels, which were applied by different stress amplitudes of 10.5 kN, 12 kN, and 13.5 kN. In comparison, the fractured surface from the higher stress amplitude of 13.5 kN showed a smaller burnished, smooth region and a larger granular, rough region, compared to the lower stress amplitude of 10.5 kN and 12 kN. According to past researchers [45,46], a larger percentage of the cross-section showed fatigue crack growth if lower nominal stress was likely applied to the material. However, a smaller percentage of the surface shows fatigue crack growth if higher nominal stress was likely applied to the material. Besides the magnitude of the applied stress, the stress concentration (notch) and fracture toughness of the material also play a similar role to the cross-section’s percentage of the crack surface.

Fig. 25(b), Fig. 26(b), and Fig. 27(b) show different types of specimens; uncoated steel, WC-12Co coated steel and WC-10Ni coated steel, which was applied at the same stress amplitude of 12 kN. From the observation, the uncoated steel shows the largest burnished, smooth region compared to the WC-12Ni coated steel and WC-12Co coated steel. This is because the notch surface formed by the coated steel due to the HVOF process caused a higher stress concentration and lead to a faster fracture. According to L. O. A. Affonso [46],

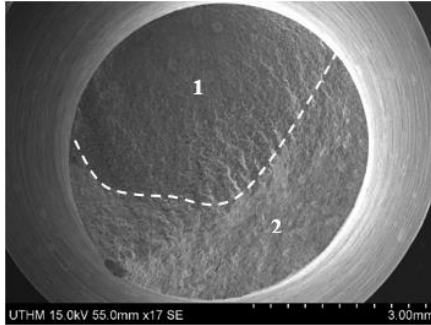
stress concentration on the component surface results in faster propagation of the cracks close to it. This will cause it to be fractured faster than a normal specimen. The faster fracture resulted in a smaller fatigue crack region and a larger final fracture region.



(a)

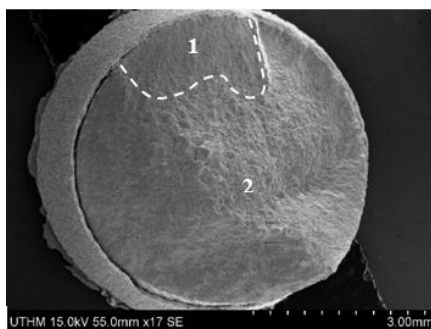


(b)

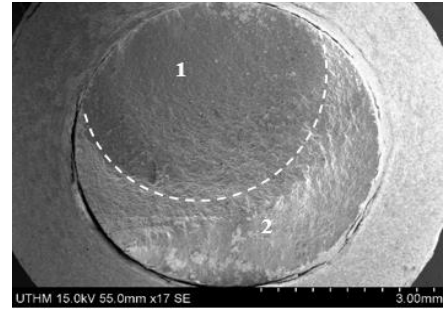


(c)

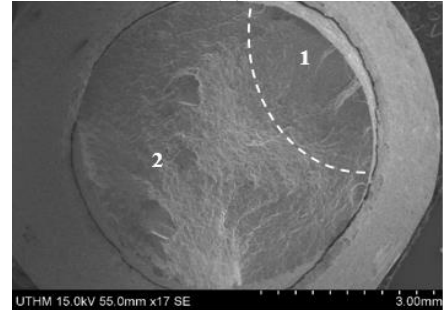
Fig. 25:The fractured surface of uncoated steel with a magnification of 17x at a stress amplitude of; (a) 13.5 kN, (b) 12 kN, (c) 10.5 kN



(a)

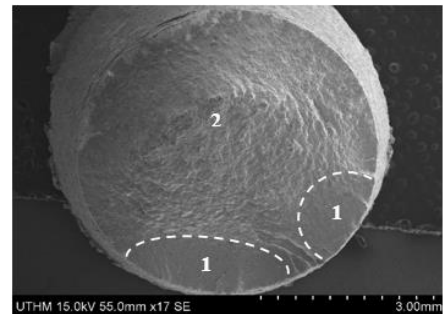


(b)

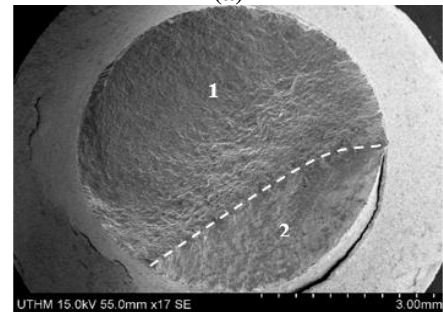


(c)

Fig. 26:The fractured surface of WC-12Co coated steel with a magnification of 17x at a stress amplitude of; (a) 13.5 kN, (b) 12 kN, (c) 10.5 kN



(a)



(b)

Fig. 27:The fractured surface of WC-10Ni coated steel with a magnification of 17x at a stress amplitude of; (a) 13.5 kN, (b) 12 kN

Fig. 28 shows the fractured surface of WC-10Ni coated steel with a magnification of 17x at a stress amplitude of 12 kN; meanwhile, Fig. 29 and Fig. 30 represent the higher

magnification (40x) image at certain regions, labeled as 3 and 4. From Fig. 29, many initial cracks can be seen near the upper right outer perimeter. These are shown by somewhat radial lines, often called “ratchet marks”, extending around the upper left perimeter. The initial cracking process began at the surface and then propagated towards the inside of the specimen. According to G. A. Pantazopoulos [47], cracks usually nucleate at or near-surface because inelastic deformation is easier at the surface. Intrusion or extrusion develops on the surface, stresses or strains from external loads are usually greatest on the surface, while stress concentration from manufacturing processes often exists on the surface, and environmental attacks such as corrosion occur on the surface. However, cracks can also nucleate at non-surface areas such as at grain boundaries, inclusions, pores, and other microstructural features or discontinuities.

From Fig. 30, fatigue striation (microscopic characteristics) is observed on the fractured surface, which indicates the progression of the fracture at each load cycle. It shows the incremental growth of a fatigue crack. However, fatigue striations are not beach marks (progression marks). Beach marks (macroscopic characteristic) are produced by modification of the stress that causes the progression of the crack tip. The progression marks indicate that the fracture progression occurs in a direction that changes somewhat from time to time. Besides that, one beach mark can contain thousands of striations [48]. These striations may not be seen clearly because of significant surface rubbing and pounding during repetitive loading. They are also very nearly impossible to find in materials of high strength.

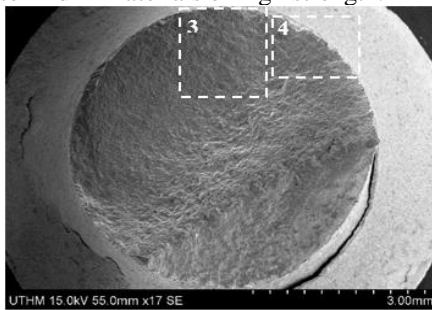


Fig. 28:The fractured surface of WC-10Ni coated steel with a magnification of 17x at a stress amplitude of 12 kN

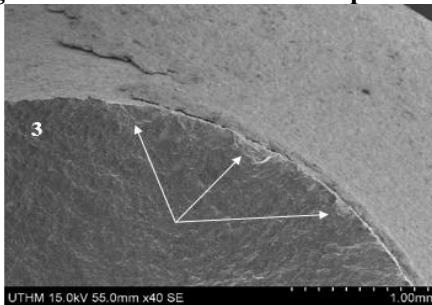


Fig. 29:Fatigue initiation at the fractured surface of WC-10Ni coated steel with a high magnification of 40x at a stress amplitude of 12 kN

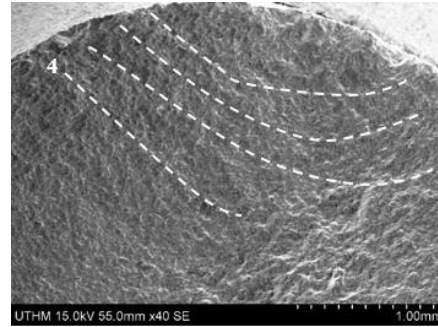


Fig. 30: Fatigue striation at the fractured surface of WC-10Ni coated steel with a high magnification of 40x at a stress amplitude of 12 kN

With reference to Fig. 31, multiple crack initiations in different regions could be observed. According to J. G. La Barbera-Sosa *et al.* [7], the multiple crack initiations were due to the notch or cracks formed by the high-velocity impact of the powder particle from the HVOF process. The notch and cracks produced at the periphery of the substrate encourage multiples of crack initiations to occur.

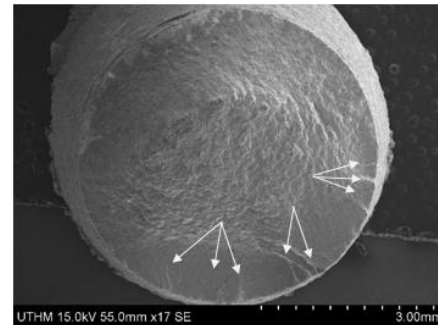


Fig. 31: Multiple crack initiation at the fractured surface of WC-10Ni coated steel with a magnification of 17x at a stress amplitude of 13.5 kN

IV. CONCLUSION

This paper aims to study the effect of WC-12Co and WC-10Ni high-velocity oxy-fuel coatings on the fatigue behaviour of S50C steel. The result showed that WC-12Co coatings reduced the fatigue strength of the S50C steel by 17%. Meanwhile, WC-10Ni coatings were reduced by 3.2%. The reduction was due to an increment of the grain size caused by the HVOF coating. In the relation between the tensile and fatigue, the fatigue ratio value, 0.36, was lower than the expected value, 0.5, because of the additional correction factor from the ‘machined’ surface finish of S50C steel. From the fractographic analysis, two clear, distinct regions, which are burnished and granular, can be seen. As the stress amplitude increased, the total burnished area decreased, indicating the reduction of the cross-section of the fatigue crack region. On the other hand, coated steel shows a smaller burnished region compared to uncoated steel due to the notch surface formed by the coated steel from the HVOF

coating process. It caused a higher stress concentration, which leads to a faster fracture.

On the other hand, the tensile and yield strength of the S50C steel decreased due to the increment of the grain size from the high-temperature effect of HVOF coating. In comparison between the coatings, the tensile and yield strength of the WC-10Ni coated steel are higher than WC-12Co coated steel because the grain size of the WC-10Ni coated steel is finer than WC-12Co coated steel. From the fractographic analysis, clear voids, spherical dimples, and cleavage facets can be found, which indicates that all uncoated, WC-10Ni and WC-12Co coated steels underwent a “moderate” ductile fracture during the tensile loading.

ACKNOWLEDGMENT

Communication of this research is made possible through monetary assistance by Universiti Tun Hussein Onn Malaysia and the UTHM Publisher's Office via Publication Fund E15216.

REFERENCES

- [1] R. J. Talib, S. Saad, M. R. M. Toff, and H. Hashim, Thermal spray coating technology - a review,” *Solid State Sci. Technol.*, 11(1)(2003) 109–117.
- [2] M. Oksa, E. Turunen, T. Suhonen, T. Varis, and S.-P. Hannula, Optimization and characterization of high-velocity oxy-fuel sprayed coatings: techniques, materials, and applications, *Coatings*, 1(1)(2011) 17–52.
- [3] P. K. Katiyar, P. K. Singh, R. Singh, and A. L. Kumar, Modes of failure of cemented tungsten carbide tool bits (WC/Co): a study of wear parts, *Int. J. Refract. Met. Hard Mater.*, 54(2016) 27–38.
- [4] I. Hulka, D. Utu, V. A. Serban, M. L. Dan, V. Matikainen, and P. Vuoristo, Corrosion Behavior of WC-Ni Coatings Deposited by Different Thermal Spraying Methods, 60(74) 2015.
- [5] R. C. Souza, M. P. Nascimento, H. J. C. Voorwald, and W. L. Pigatin, The effect of WC-17Co thermal spray coating by HVOF and hard chromium electroplating on the fatigue life and abrasive wear resistance of AISI 4340 high strength steel, *Corros. Rev.*, 21(1)(2003) 75–96.
- [6] G. S. Junior, H. J. C. Voorwald, L. F. S. Vieira, M. O. H. Cioffi, and R. G. Bonora, Evaluation of WC-10Ni thermal spray coating with shot peening on the fatigue strength of AISI 4340 steel, *Procedia Eng.*, 2(1)(2010) 649–656.
- [7] J. G. La Barbera-Sosa et al., Fatigue behavior of a structural steel coated with a WC-10Co-4Cr/Colmonoy 88 deposit by HVOF thermal spraying, *Surf. Coatings Technol.*, 220(2013) 248–256.
- [8] R. G. Bonora, H. J. C. Voorwald, M. O. H. Cioffi, G. S. Junior, and L. F. V. Santos, Fatigue in AISI 4340 steel thermal spray coating by HVOF for aeronautic application, *Procedia Eng.*, 2(1)(2010) 1617–1623
- [9] E. S. Puchi-Cabrera et al., Fatigue behavior of an SAE 1045 steel coated with Colmonoy 88 alloy deposited by HVOF thermal spray, *Surf. Coatings Technol.*, 205(4)(2010) 1119–1126.
- [10] A. C. Murariu, A. V. Cernescu, and I. A. Perianu, The effect of saline environment on the fatigue behaviour of HVOF-sprayed WC–CrC–Ni coatings, *Surf. Eng.*, 34(10)(2018) 755–761.
- [11] E. F. Rejda, D. F. Socie, and B. Beardsley, Fatigue behavior of a plasma-sprayed 8%Y2O3-ZrO2thermal barrier coating, *Fatigue Fract. Eng. Mater. Struct.*, 20(7)(1997) 1043–1050.
- [12] M. P. Nascimento, R. C. Souza, I. M. Miguel, W. L. Pigatin, and H. J. C. Voorwald, Effects of tungsten carbide thermal spray coating by HP/HVOF and hard chromium electroplating on AISI 4340 high strength steel, *Surf. Coatings Technol.*, 138(2–3)(2001) 113–124.
- [13] H. J. C. Voorwald, L. F. S. Vieira, and M. O. H. Cioffi, Evaluation of WC-10Ni thermal spraying coating by HVOF on the fatigue and corrosion AISI 4340 steel, *Procedia Eng.*, 2(1)(2010) 331–340.
- [14] T. C. Totemeier, R. N. Wright, and W. D. Swank, Mechanical and physical properties of high-velocity oxy-fuel-sprayed iron aluminide coatings, *Metall. Mater. Trans. A*, 34A(10)(2003) 2223–2231.
- [15] A. Ibrahim and C. C. Berndt, The effect of high-velocity oxygen fuel, thermally sprayed WC-Co coatings on the high-cycle fatigue of aluminium alloy and steel, *J. Mater. Sci.*, 33(12)(1998) 3095–3100.
- [16] E. S. Puchi-Cabrera et al., Fatigue behavior of AA7075-T6 aluminum alloy coated with a WC-10Co-4Cr cermet by HVOF thermal spray, *Surf. Coatings Technol.*, 220(2013) 122–130.
- [17] H. Okada, Y. Uematsu, and K. Tokaji, Fatigue behavior in AZ80A magnesium alloy with DLC/thermally sprayed WC-12Co hybrid coating, *Procedia Eng.*, 2(1)(2010) 283–290.
- [18] J. Kawakita, S. Kuroda, and T. Kodama, Evaluation of through-porosity of HVOF sprayed coating, *Surf. Coatings Technol.*, 166(1)(2003) 17–23.
- [19] R. Nieminen, P. Vuoristo, K. Niemi, T. Mäntylä, and G. Barbezat, Rolling contact fatigue failure mechanisms in plasma and HVOF sprayed WC-Co coatings, *Wear*, 212(1)(1997) 66–77.
- [20] N. A. Ahmad, Z. Kamdi, A. Latif, and M. Tobi, Wear and corrosion behavior of tungsten carbide-based coating on carbon steel, *Int. J. Integr. Eng.*, 10(4)(2018) 119–125.
- [21] ASTM Standard E8/E8M. Standard Test Methods for Tension Testing of Metallic Materials. West Conshohocken: ASTM International, 2009.
- [22] ASTM Standard E466. Conducting Force Controlled Constant Amplitude Axial Fatigue Tests of Metallic Materials. West Conshohocken: ASTM International, 2015.
- [23] T. A. Ben Mahmud, G. C. Saha, and T. I. Khan, Mechanical property changes in HVOF sprayed nano-structured WC-17wt.%Ni(80/20)Cr coating with varying substrate roughness, *IOP Conf. Ser. Mater. Sci. Eng.*, 60(2014) 1–8.
- [24] S. Banerjee, P. C. Chakraborti, and S. K. Saha, An automated methodology for grain segmentation and grain size measurement from optical micrographs,” *Measurement*, 140(2019)142–150.
- [25] A. A. Azeez, Fatigue Failure and Testing Methods, Dissertation of Bachelor, HAMK University of applied sciences, 2013.
- [26] Y. Murakami, *Metal Fatigue: Effects of Small Defects and Nonmetallic Inclusions*. Kyushu University, Japan: Elsevier, 2002.
- [27] B. Wielage, H. Pokhmurska, A. Wank, G. Reisel, S. Steinhäuser, and M. Woezel, Influence of thermal spraying method on the properties of tungsten carbide coatings, in *Proceedings of the Conference on Modern Wear and Corrosion Resistant Coatings Obtained by Thermal Spraying*, (2003) 20–21.
- [28] L. Gu, J. Huang, Y. Tang, C. Xie, and S. Gao, Influence of different post treatments on microstructure and properties of WC-Co cemented carbides, *J. Alloys Compd.*, 620(2015) 116–119.
- [29] J. M. Guilemany, J. Nutting, J. R. Miguel, and Z. Dong, Microstructure formation of HVOF sprayed WC-Ni coatings deposited on low alloy steel, *Mater. Manuf. Process.*, 12(5)(1997) 901–909.
- [30] Y. M. Zou, Y. S. Wu, J. Z. Wang, Z. G. Qiu, and D. C. Zeng, Preparation, mechanical properties and cyclic oxidation behavior of the nanostructured NiCrCoAlY-TiB2 coating, *Ceram. Int.*, 44(16)(2018) 19362–19369.
- [31] D. Tejero-Martin, Z. Pala, S. Rushworth, and T. Hussain, Splat formation and microstructure of solution precursor thermal sprayed Nb-doped titanium oxide coatings, *Ceram. Int.*, 46(4)(2020) 5098–5108.
- [32] J. G. La Barbera-Sosa et al., Microstructural and mechanical characterization of Ni-base thermal spray coatings deposited by HVOF, *Surf. Coatings Technol.*, 202(18)(2008) 4552–4559.
- [33] N. W. Satya and W. Winarto, Microstructure, hardness, and surface cracks evaluation of HVOF-sprayed stellite-1 coating applied on steam turbine blade, *Key Eng. Mater.*, 833 KEM(2020) 80–84.
- [34] G. Bolelli, L. Lusvardi, and M. Barletta, HVOF-sprayed WC-CoCr coatings on Al alloy: Effect of the coating thickness on the tribological properties, *Wear*, 267(5–8) 944–953.

- [35] M. Jadidi, S. Moghtadernejad, and A. Dolatabadi, A comprehensive review on fluid dynamics and transport of suspension/liquid droplets and particles in High-Velocity Oxygen-Fuel (HVOF) thermal spray, *Coatings*, 5(4)(2015) 576–645.
- [36] W. D. Callister, *Materials science and engineering: An introduction*, 7th ed. New York: John Wiley & Sons, 2007.
- [37] A. W. Zia, Z. Zhou, P. W. Shum, and L. K. Y. Li, The effect of two-step heat treatment on hardness, fracture toughness, and wear of different biased diamond-like carbon coatings, *Surf. Coatings Technol.*, 320(2017) 118–125.
- [38] V. K. Satish, Chapter 8. Failure, in *Material Science*, Dept. of Mechanical Engineering, Indian Institute of Science, Bangalore, 2009.
- [39] C. Pandey, A. Giri, and M. M. Mahapatra, Evolution of phases in P91 steel in various heat treatment conditions and their effect on microstructure stability and mechanical properties, *Mater. Sci. Eng. A*, 664(2016) 58–74.
- [40] S. Yan and X. Zhao, A fracture criterion for fracture simulation of ductile metals based on micro-mechanisms, *Theor. Appl. Fract. Mech.*, 95(2018) 127–142.
- [41] R. I. Stephens, A. Fatemi, R. R. Stephens, and H. O. Fuchs, *Metal Fatigue in Engineering*, 2nd edition. Wiley Interscience, 2000.
- [42] S. Kalpakjian, *Manufacturing Engineering and Technology*, 3rd ed. Addison-Wesley Publishing Co., 1995.
- [43] R. C. Juvinall and K. M. Marshek, *Fundamentals of Machine Component Design*, 2nd ed. New York: John Wiley and Sons, 1991.
- [44] J. Siegl, I. Nedbal, and J. Kunz, Fractographic study of fatigue processes, in *Fracture Damage of Structural Parts*, (2004) 165–172.
- [45] G. Jacoby, Fractographic methods in fatigue research, *Exp. Mech.*, 5(3)(1965) 65–82.
- [46] L. O. A. Affonso, *Machinery Failure Analysis Handbook: Sustain Your Operations and Maximize Uptime*, vol. 1. 2007.
- [47] G. A. Pantazopoulos, A short review on fracture mechanisms of mechanical components operated under industrial process conditions: Fractographic analysis and selected prevention strategies, *Metals (Basel)*, 9(2)(2019).
- [48] R. W. Hertzberg, *Deformation and Fracture Mechanics of Engineering Materials*, 4th ed. New York: John Wiley and Sons, 1996.